Journal of Materials Chemistry C

Accepted Manuscript

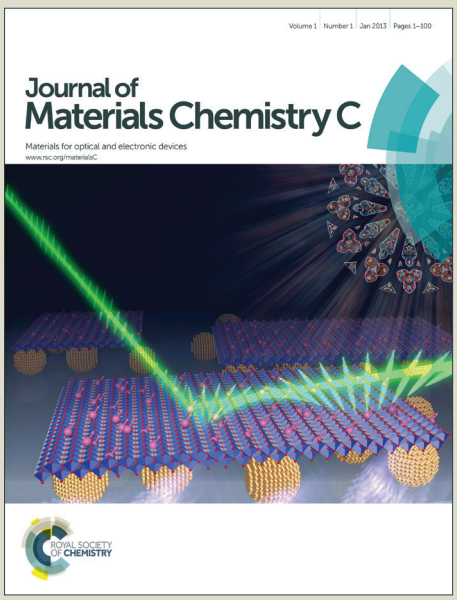

ROYAL SOCIETY OF CHEMISTRY

www.rsc.org/materialsC

Phthalimide-Thiophene-based Conjugated Organic Small Molecules with High Electron Mobility

Jon-Paul Sun,[a] Arthur D. Hendsbee,[b] Ala'a F. Eftaiha,[a,b] Casper Macaulay,[b] Lesley R. Rutledge,[b] Gregory C. Welch[b]* and Ian G. Hill[a]*

A series of low-cost phthalimide end-capped oligothiophene small molecules with variations to the terminal alkyl chain and number of thiophene units in the conjugated core have been synthesized and investigated. All molecules exhibit H-aggregation in the solid-state but different crystal structures and electronic properties, showing that subtle chemical modifications can result in dramatic changes to molecular self-assembly. Field-effect transistors display high electron mobilities of up to 0.2 $cm^2 V^{-1} s^{-1}$.

1. Introduction

High performance, electron-transporting (n-channel) organic materials have a wide variety of applications, including organic photovoltaics (OPVs),[1–4] organic field-effect transistors (OFETs),[5–7] organic light-emitting diodes (OLEDs),[8] and charge storage devices.[9] A candidate material to be used in these devices should have high charge carrier mobility, facile and cost effective synthesis, ability to collect and inject charge at interfaces, and be oxygen and moisture stable under operating conditions.[10] Since carrier transport in conjugated organic systems occurs via hopping between adjacent molecules, efficient charge transfer relies on strong coupling between adjacent π-systems,[11] which can be achieved through favorable self-assembly. Controlling self-assembly through chemical modification is a powerful tool for realizing high performing organic electronic materials.[12]

Conjugated organic materials, both polymeric and molecular have displayed a tendency to assemble into ordered domains on the nanometer scale via non-covalent interactions.[13–15] Oligothiophenes are a thoroughly studied class of such materials that have been present in several state of the art devices including both OPVs and OFETs.[16] Both p-channel and n-channel oligothiophenes are well represented in the literature,[17–20] with n-channel devices exhibiting electron mobility values of up to 4.6 $cm^2 V^{-1} s^{-1}$.[21] In addition to the high carrier mobility values demonstrated, several desirable properties are boasted by this class of materials, including the possibility for ambipolar charge transport,[22–24] tunable synthesis,[25,26] and durability.[27,28] The air stability of functionalized oligothiophenes has attracted considerable attention for OFET applications.[19,29–32] This stability can be explained by their relatively low-lying lowest unoccupied molecular orbitals (LUMOs) making them resistant to charge trapping by oxygen species.[17] This effect is further enhanced by adding electron-withdrawing end-groups to further lower LUMO levels, or by creating steric hindrance through tight molecular packing or the addition of bulky substituents to create physical barriers to ambient H_2O and O_2. Furthermore, lowering the LUMO aids in promoting electron injection at the metal contacts in OFETs.[10]

Oligomeric thiophene compounds with electron-withdrawing end-caps to promote self-assembly and tailor energy levels are of current interest in the literature. In this context, several strategies have been reported to improve the performance of oligothiophene semiconductors by incorporating electron-deficient groups (such as asbenzothiadiazole,[33] isoindigo,[34] cyano and dicyano-vinyl groups,[35,36] pyridino units,[37] perfluoroalkyl substituents,[38] etc…). The strong electron-withdrawing nature of imides also makes them excellent candidates for functionalizing aromatic rings to create building blocks for electron-deficient electroactive materials. To date, the majority of materials using such building blocks place the imide moieties in the core of the molecule or as acceptors in D-A polymers, resulting in the imide groups lying perpendicular to the π-conjugated backbone. However, there have been limited reports of imide groups being used as end-capping units, in a configuration parallel to the backbone. Recently, in one such report Durso *et al.* have demonstrated that stable, high mobility, n-channel OFETs can be fabricated using oligothiophenes with thieno(bis)imide end-capping units, with reported mobilities of 0.3 $cm^2 V^{-1} s^{-1}$.[41] While the thieno(bis)imide building block is an attractive unit, it suffers from a difficult multi-step synthesis requiring alkyl-Li reagents, cryogenic-temperature reaction conditions, the use of CO_2 and $SOCl_2$, and problematic acid/base work-up conditions. A simpler and more sustainable alternative needs to be sought out. Conversely, phthalimide is an under-utilized building block for which the functionalized phthalimide precursor, 4-bromophthalic anhydride, can be purchased for less than $1 per gram (TCI), and can easily be converted to the imide via simple condensation reactions. Functionalization at the nitrogen atom is easily controlled via rational choice of the amine used in the imide forming

step, allowing greater control over the solubility properties of the molecule. Thus, this unit presents itself as a cost-effective and readily available material for constructing organic functional materials.

Based on these discoveries, we have chosen to investigate oligothiophene compounds functionalized with the electron-deficient phthalimide building block, with the expectation that the strong electron-withdrawing nature of the imide groups would lead to desirable n-channel OFET performance. Furthermore, we systematically changed the length of the terminal alkyl chains and the number of thiophenes in the core, showing that subtle chemical modifications affect the self-assembly of these compounds, and the resulting electron transport capabilities.

2. Experimental

2.1 UV-Visible Spectroscopy (UV-vis)

All UV-vis spectra were recorded with an Agilent Cary 60 Spectrophotometer at room temperature. All solution UV-vis experiments were run using $CHCl_3$ as a solvent in teflon capped 1 mm quartz cuvettes. Films were prepared by spin coating solutions from $CHCl_3$ onto glass substrates cut from corning microscope slides at 1000 rpm for 10 seconds. Annealed films were annealed at 100 °C for 10 min by direct mounting on a VWR hotplate/stirrer.

2.2 Differential Scanning Calorimetry (DSC)

DSC was performed on a TA instruments Q-1000 DSC with compressed air as the purging gas.

2.3 Single Crystal X-Ray Diffraction

X-ray crystallographic data collection was carried out using a Bruker APEX II CCD with a Mo K-α source (30 mA, 50 kV) and omega scans. Crystals were mounted on X-ray transparent polymer mounts. Cell refinement was done using SAINT and data reduction using SAINT. Structure identification was completed using SHELXS97. Structure refinement software packages used included SHELXL97 and Olex2.

2.4 Ultraviolet Photoelectron Spectroscopy (UPS)

0.2 % and 0.4 % w/v solutions of each compound were spin coated from $CHCl_3$ at 5000 rpm, to produce films of two different thicknesses on top of polished float glass coated with 80 nm of ITO (Delta Technologies). All films were prepared in air and immediately transferred to the UPS chamber, where they were held under high vacuum for several hours prior to measuring. The UPS analysis chamber was equipped with a hemispherical energy analyzer (Phoibos 150) and was maintained at a base pressure of 10^{-10} mbar. The UPS measurements were carried out using a He I ($h\nu$ = 21.22 eV) source. A sample bias of -3 V was used to measure the onset of photoemission. Reproducibility of UPS spectra between the two film thicknesses was confirmed for each compound.

2.5 Device Fabrication and Testing

n-channel bottom-gate top-contact transistors were formed on heavily doped Si wafers (n-type; arsenic; <0.035 Ω cm) with 300 nm thermal SiO_2. Si coupons were sonicated in isopropyl alcohol, blown dry with compressed air, followed by UV-ozone treatment for 20 min. Cytop dielectric was prepared by spin coating 3 parts Cytop CTL-809 M dissolved in 14 parts CTSolv-180 at 5000 rpm for 60 s on top of the 300 nm SiO_2. Capacitors were fabricated by depositing metal electrodes through a stencil mask to measure the specific capacitance, which was found to be 10.7 nF cm^{-2}. Following dielectric preparation, the samples were transferred to a vacuum deposition system (base pressure 10^{-6} mbar). 30 nm of each compound was deposited through a stencil mask at 0.02-0.05 nm s^{-1} onto the coupons held at 100 °C. The samples were allowed to cool to <40 °C before vacuum was broken, and a source-drain stencil mask was aligned with the active semiconductor. Aluminum source-drain contacts were deposited at a rate of 0.05 nm s^{-1} to a thickness of 50 nm. Each coupon contained an array of 24 transistors with channel lengths ranging from 25 μm to 250 μm and widths between 0.5 mm and 1.5 mm. After metal deposition, the samples were briefly exposed to air again for a few minutes before transferring to an Ar glove box for testing. Two Kiethley 236 source-measure units were used to measure the current-voltage characteristics of the devices.

3. Results and Discussion

3.1 Molecular Design and Synthesis

Previously, we have reported on the optimized synthesis of the small molecule 5,5'-(2-octyl)isoindoline-1,3-dione bithiophene (**1**),[42] which is composed of a bithiophene core with *n*-octyl substituted phthalimide end-capping units. This molecule exhibited a blue shift in the absorbance maximum upon transitioning from solution to thin-film. Single crystal X-ray diffraction revealed that **1** displayed strong face-to-face π-stacking in the solid state. This packing orientation, often referred to as H-aggregation,[43] has been demonstrated in many systems with high charge carrier mobilities.[27,44–50] In an effort to understand the extent to which phthalimide-thiophene materials undergo H-aggregation, we systematically varied the length of the thiophene core and terminal alkyl chains. Target molecules are shown in Figure 1.

The terminal alkyl chain length was varied from C_4 to C_6 to C_8 in order to study the effect of chain length on solubility characteristics and self-assembly properties, while the number of thiophene units in the core was both increased (**4**) and decreased (**5**) to examine the effect of extended π-conjugation on optoelectronic properties. Compounds **1**, **2**, and **3** were synthesized using optimized microwave-assisted direct arylation procedures, while compounds **4** and **5** were synthesized using conventional Stille cross-coupling reactions. All compounds were isolated as yellow or orange solids and fully characterized by NMR and mass spectroscopy. Full synthetic details and spectra can be found in the supporting information.

3.2 Solution and Solid-State Optical Properties

For a comparison to compound **1**, the optical absorbance and emission spectra of compounds **2**-**5** were determined in $CHCl_3$ solution (Figure S6, data in Table 1). Not surprisingly, compounds **1**-**3** with the same π-conjugated backbone have similar absorbance profiles with maxima at 424, 425, and 428 nm, respectively. Interestingly, larger differences were observed in the emission maxima, measured at 508, 515, and 523 nm, for compounds **1**-**3**, respectively. The progressive increase in Stokes shift with decreasing alkyl chain length is suggestive of less energetic structural reorganization upon photoexcitation for compounds with longer alkyl chains. Comparing **1** to **4** and **5**, increasing the number of thiophene core units from two to three red-shifts the absorbance maximum from 424 nm (**1**) to 450 nm (**4**), while decreasing the number of thiophene core units to one results in a blue shift to 390 nm (**5**). The emission profiles of **1**, **4**, and **5** are shifted to longer wavelengths with increasing number of thiophene units, consistent with the red-shifted absorption maxima. Interestingly, the Stokes shift decreases with decreasing number of thiophene core units, from 88 nm for **4** to 84 nm for **1**, to 75 nm for **5**, indicating greater structural freedom in compound **4**.

Compounds **1**, **2**, **4**, and **5** were found to be sufficiently soluble to allow for thin-film formation via spin coating from $CHCl_3$ solution. Compound **3** (*n*-butyl) was not sufficiently soluble at room temperature to ensure a viscous enough solution to promote substrate wetting via spin-casting. In order to obtain uniform thin films of compound **3**, higher concentration solutions in $CHCl_3$ were cast at 50 °C.

The thin-film absorption (compared to solution absorption) is shown in Figure 2. For all compounds a red shift in the onset of absorption is observed, while a blue shift in the maximum absorption is observed. This blue shift is most pronounced in compounds **1**, **2**, and **4**, all with long alkyl chains and containing two or more thiophene cores. As previously reported,[42] such behavior can be attributed to strong face-to-face π-stacking in the solid state (H-aggregation), and is rare for symmetrical compounds.

Comparing compounds **1**-**3**, a decrease in blue shift was observed with decreasing alkyl chain length, from 39 to 35 to 28 nm, respectively. Comparing compounds **1**, **4** and **5**, an increase in thiophene units from two (**1**) to three (**4**) results in an increase in blue shift from 39 to 50 nm. Decreasing the number of thiophenes to one (**5**) decreases the blue shift to 15 nm.

3.3 Thin Film X-ray Characterization and Optical Microscopy

To better understand the H-aggregation behavior observed in the absorbance spectra, we used X-ray diffraction and optical microscopy to characterize the crystalline properties of thin films of **1**-**5**. In a similar finding to Durso *et al.*,[51] we found that the 2-thienyl derivative (**1**) readily crystallized from solution and the odd-numbered thienyl derivatives (**4** and **5**) simply formed a powder from solution. Owing to the stronger tendency for 2-thienyl derivatives to crystallize, we further evaluated the solution behaviors of these materials. The solubility of compounds **1**, **2**, and **3**, featuring *n*-octyl, *n*-hexyl and *n*-butyl terminal alkyl chains, respectively, was determined in $CHCl_3$. The room temperature solubilities followed a linear trend, where the solubility increases by approximately 7 mg mL^{-1} for each two-carbon extension of the terminal alkyl chain (*n*-butyl: 0.4 mg mL^{-1}; *n*-hexyl: 7.4 mg mL^{-1}; *n*-octyl: 15.2 mg mL^{-1}).

Films of compounds **1**-**3** produced using spin coating did not produce diffraction peaks above the signal to noise threshold when exposed to X-rays and so drop casting was used. Thin films were prepared from the maximum concentrations obtainable at 58 °C in $CHCl_3$ (50 mg mL^{-1}, 13.2 mg mL^{-1} and 1.15 mg mL^{-1} for compounds **1**, **2** and **3**,

respectively). Drop casting at this temperature allowed for more concentrated solutions that were necessary in order to create films with appropriate thickness for film X-ray analysis and optical microscopy. Film X-ray analysis and optical microscopy of evaporated thin films were also found to be prohibitive. All drop-cast films of compounds **1**-**3** exhibited a poor tendency to coat the entire substrate after drying in air, although substrates with compound **1** featuring *n*-octyl chains were noticeably more uniformly coated, presumably due to the higher starting concentration of the drop casting solution. Thin films of compounds **1** and **2** were both apparently crystalline to the naked eye, while compound **3** exhibited a more amorphous texture (Figure 3).

Under the optical microscope the differences in the films created by drop casting became much more apparent. Compound **1**, for instance, formed long, orange needle-like crystals which were several hundreds of micrometers in length (Figure 3a). Compound **2**, which was also visibly crystalline, formed smaller, orange needle-like crystals approximately 100-200 μm in length (Figure 3b). Compound **3**, which was not crystalline to the naked eye, formed extremely small orange crystals ~20 μm in length (Figure 3c). It should also be noted that if a less concentrated solution of compound **1** was prepared for drop casting (10 mg mL^{-1} vs. 50 mg mL^{-1}) then a different structure is observed under the optical microscope where no needle structures are formed and instead polygonal shaped crystals form and aggregate into clusters at the edge of the glass substrate (Figure 3d, attributed to the 'coffee ring' Marangoni effects).[52] Reducing the concentration of solutions of **2**, resulted in drop-cast films exhibiting only small regions of microcrystalline samples (Figure 3e). This drastic change in crystalline behavior with subtle modifications to the alkyl chain length highlights the importance of understanding the complex interplay between hydrogen bond, Van der Waals, and π-π interactions.

In order to further examine the crystalline properties of the films, X-ray diffraction was performed on the drop-cast thin film samples of compounds **1**-**3** (Figure 3). The diffraction patterns from the films are compared with predicted powder patterns from single crystal data (Figure S7) in order to determine if preferential orientation occurs on the substrate during drop-casting. Compound **1** displayed several sharp diffraction peaks at angles of 3.9°, 4.65°, 7.15°, 7.55°, 12.1°, 12.85°, and 19.85°, and showed approximately equal intensities for signals coming from the *h*00, 0*k*0 and 00*l* families of planes, indicating that the crystallites were randomly oriented on the substrate, consistent with the optical microscopy images (Figure 3a). Compound **2** which displayed only 5 diffraction peaks above the signal to noise threshold at angles of 5.45°, 6.20°, 8.45°, 11.45°, 19.15°, also showed no preferential orientation with respect to the substrate as the peak intensities were similar for different diffracting sets of planes. Compound **3** did not display any diffraction peaks above the signal to noise threshold, possibly due to the presence of extremely small crystalline domains that could not be detected using simple powder X-ray diffraction techniques. The expected powder patterns were produced from the experimental single crystal data (*vide infra*) and showed good agreement with the obtained diffraction patterns, although in general more peaks were predicted than were observed (Figure S7). Interestingly, the most intense powder diffraction peak obtained from samples of **1** was not predicted from the single crystal pattern, possibly indicating the presence of a second crystalline phase not present in the single crystal data. This observation, combined with the presence of two apparently different crystal morphologies under the optical microscope is a good indication that a second crystal phase likely exists for compound **1**.

Several single crystals (needles and polygons, Figure 3) of this compound were analyzed via single crystal X-ray diffraction in order to determine if a different phase was present but none was found.

3.4 Single Crystal X-ray Diffraction

The extent of crystalinity is not the only factor affecting charge transport in organic molecules; another crucial factor is the degree of orbital overlap between adjacent molecules. To this end, we grew single crystals for X-ray diffraction in order to further elucidate the solid-state packing arrangements of small molecules **1**-**5**. A clear trend was apparent in that ability of the molecules with longer alkyl chains to form single-crystals was superior. Both small molecules **1** and **2** were found to readily crystalize from a slowly evaporating solution in dichloromethane, although **1** produced the largest crystals with the least effort. After extensive attempts, single crystals of **3** could not be obtained, consistent with the microcrystalline structures observed in the optical images. Single crystals of compounds **4** and **5** were also not obtained after multiple crystallization attempts. Single crystal analysis of the two compounds which could be readily crystalized (**1** vs **2**) revealed a striking difference in the packing arrangements that can only be caused by a difference in alkyl chain length. Illustrative crystal structures of compounds **1** and **2** are shown in Figure 4.

The primary difference between the the octyl substituted derivative (**1**) and the hexyl derivative (**2**) is that a herringbone-like packing motif referred to as the γ-structure is observed for **1**,[53] which has a 'herringbone' angle of 76° and pitch and roll angles, as defined by Curtis *et. al*,[54] of 28° and 54° along the long and short axes, corresponding to shifts in the π-stacking of 1.6 and 4.1 Å, respectively. A herringbone-like packing motif is interestingly *not* observed for **2**, which instead arranges into columnar stacks with pitch and roll angles of 31° and 46° along the long and short axes

of the molecule, corresponding to shifts in the π-stacking of 1.9 and 3.4 Å, respectively. It is commonly noted in the literature that cofacial herringbone-type structures such as the γ-configuration, offer advantages in charge transport capability when compared to purely 1-D columnar stacking arrangements, as cofacial herringbone-type configurations are predicted to provide a more favorable geometry for multi-dimensional charge transport.[55–57] The octyl derivative features a slightly shorter spacing between stacked aromatic units compared to the hexyl derivative (3.01 vs 3.24 Å). Crystallographic data for compounds **1** and **2** can be found in Reference 42 and Table S1.

3.5 Thermal Analysis

Electronic devices often operate at elevated temperatures, due to incident radiation (solar cells) or due to internal power dissipation (resistive circuitry, OFETs, OLEDs, etc…). Therefore it is important to test the thermal properties of new conjugated organic compounds before they can be touted as good candidates for organic electronic devices. Differential Scanning Calorimetry (DSC) was used to determine the melting and crystallization points of compounds **1**-**5** (Figure S9, data in Table 2). Compounds **1**, **2** and **3** have melting points of 221 °C, 230 °C and 279 °C respectively, which are all well above the expected operating temperatures of most electronic devices. The increase in melting temperature with decrease in alkyl chain length is in good agreement with similar predictions from the literature,[58–60] indicating that the ratio of intermolecular π-π interactions is increased with respect to the weaker alkyl-alkyl interactions with shortening alkyl chain length. Compounds **1**, **2** and **3** have crystallization points of 208 °C, 215 °C and 243 °C, respectively, a trend that is expected for the same reason as is the trend in melting points. Although the lengths of the carbon chains for compounds **1**-**3** decrease in a linear fashion from C_8 to C_6 to C_4, respectively, there is a sharp increase in melting temperature for compound **3** compared to either **2** or **1**. In addition, the greatest difference between melting and crystallization temperatures can be seen for compound **3**.

Compounds **4** and **5**, featuring three and one thiophene units in the molecular core, respectively, were also studied using DSC and had melting points of 245 °C and 204 °C, and crystallization temperatures of 231 °C and 191 °C. These values are in good agreement with the previous observation regarding the ratio of intermolecular π-π interactions versus alkyl-alkyl-interactions, with compound **4**, having a larger chromophore density and thus higher melting and crystallization temperatures. Compound **4** displayed liquid crystalline features above its melting point on the DSC which were not examined in further depth in this study, however liquid crystals are of current interest to the field of organic electronics due to their innate nature to form ordered nanostructures.[61–65]

3.6 Electron Energy Level Determination

Ultraviolet photoelectron spectroscopy was used to determine the ionization energy (IE) for each compound (Figure S10, data in Table 2), spin cast as ultrathin films (~2-10 nm) from $CHCl_3$ on indium tin oxide substrates. A clear trend in going from one thiophene in the core (**5**) to two (**1**) to three (**4**) can be seen as the IEs decrease by 0.4 eV each time a thiophene unit is added to the molecule. Changes in IE between compounds **1**-**3** show much greater variation than expected considering only small alkyl chain length modifications are present, however ultrathin films of pentacenes[66–68] and sexithiophenes[69] have demonstrated that molecular orientation on the substrate surface (lying flat versus standing upright) can result in changes of this magnitude to the IE. Attempts to measure the IEs of thicker films to reduce the possible effect of molecular ordering on the substrate resulted in charging, producing unreliable results. Since the LUMO levels derived from the IEs and thin film optical band gaps (Table 3) all fall within -3.5 eV to -4.2 eV, Al source/drain contacts were determined to be appropriate for charge injection when incorporated into n-channel FET devices. Further investigation of the molecular orientation at the surface of compounds **1-3** requires synchrotron-based XRD and will be performed in a following study.

3.7 Computational Chemistry

To probe further into the optical and electronic properties of compounds **1**-**5**, density functional theory (DFT) calculations were considered within Gaussian 09.[70] In order to facilitate computation, the solubilizing chains along the conjugated backbone of **1**, **4** and **5** were truncated (represented as methyl groups), and gas-phase B3LYP/6-31G(d,p) structures were determined (Figure 5). For compounds **1**-**3**, DFT comparisons could not be made as all terminal R-groups were replaced with methyl groups.

Subsequently, the low-lying singlet excited states of **1**, **4**, and **5** were calculated for the resulting ground-state geometry using time-dependent (TD) DFT with B3LYP/6-31G(d,p).

The gas-phase geometry of **1**, **4**, and **5** shows a preferential twist between the end-cap and adjacent thiophene ring planes by ~20°, as well as ~15° twist between the central thiophene–thiophene ring planes in **1** and **4**. The HOMO and LUMO orbitals are very similarly delocalized across to entire conjugated backbone for **1**, **4**, and **5**, where the LUMO

energies for all three molecules are calculated to be the same (Table 2). However, as expected, the HOMO becomes less tightly bound as the number of thiophene rings increases, resulting in the smallest band-gap for **4** (Table 2). This same trend is reflected in the UPS derived IEs. Additionally, compound **4** has the largest dipole moment, which could be important for solid-state packing of these molecules.

The calculated (normalized) absorption spectra for the three molecules are shown in Figure S11. The transition with the largest oscillator strength corresponds to the HOMO → LUMO one-electron excitation. Also, the additional transition observed in the absorption spectra corresponds to the (S3) HOMO → LUMO+2 one-electron excitation for all three molecules. Our calculations reproduce the notable red shift of the absorbance spectra as the number of thiophene rings increase as observed with solution and thin film UV-vis.

3.8 Device Characteristics

Electron transport capabilities were measured by fabricating bottom-gate top-contact OFETs, using Al as the source/drain electrode and 300 nm SiO_2 with approximately 10 nm of Cytop as the gate dielectric. Due to the low solubility of compound **3**, vacuum thermal evaporation was used to deposit the organic layers of all devices for a comparison of electron mobilities. UV-vis absorbance measurements made on evaporated films of compounds **1**-**5** showed similar spectra to those displayed in Figure 2 (see Figure S12), indicating similar H-aggregation behavior for spin cast and evaporated films. Figure 6 shows the FET saturation transfer curves, with results summarized in Table 2. Output curves are shown in Figure S13.

Compounds **1**-**3** and **5** all have similar electron mobilities on the order of 10^{-1} cm^2 V^{-1} s^{-1}, placing them on the higher end of the spectrum of n-channel OFETs reported in the literature.[17] It is interesting to note that alkyl chain length variations between **1**-**3** resulted in very different solution crystallization properties, yet similar mobilities in evaporated films. Compound **4** exhibited a lower mobility on the order of 10^{-3} cm^2 V^{-1} s^{-1}. Since the DFT calculations show equivalent LUMO delocalization along the conjugated backbone for one, two, and three thiophene-containing compounds, the reduced mobility of **4** could be a result of the increased degree of twisting along the backbone from the additional thiophene spacer, leading to a lower degree of LUMO-LUMO overlap between adjacent molecules. The crystal packing arrangement could also have an effect on this, as exhibited by differences in mobility between **1** and **2**. However, without a crystal structure for **4** it is difficult to ascertain the cause of the decreased performance. Additionally, **4** suffered from a relatively high current in the off state, and a higher subthreshold voltage swing, both of which are consistent with a high density of gap states.

4. Conclusion

A series of five phthalimide/thiophene-based small organic molecules were synthesized, with subtle differences in regards to the length of the terminal alkyl chain as well as the number of thiophene units in the conjugated backbone. These small chemical modifications resulted in significant changes to the crystalline packing structure. Through single crystal XRD, UV- vis absorbance, and DFT calculations, we have shown that these compounds have a tendency to H-aggregate, forming favorable π-stacking behavior with delocalized LUMOs. In spite of the differences in crystal structures determined for compounds **1** and **2**, high OFET electron mobilities were attained for four of the five compounds (~10^{-1} cm^2 V^{-1} s^{-1}). Compound **4**, with three thiophene units, showed a decreased electron mobility (~10^{-3} cm^2 V^{-1} s^{-1}), although the reason for this could not be determined at this time. Regardless, the bithiophene core with phthalimide end-capping units has been demonstrated to be an effective framework for electron-transporting organic small molecules. This structure utilizes cost-effective building blocks that can be put together in a simple and modular fashion, utilizing atom-efficient pathways involving direct arylation in microwave conditions. The small energy budget of this class of materials makes it attractive for scalable integration into commercial devices. Further studies on this framework involving additional modifications for enhanced OFET and OPV performance are currently underway.

Acknowledgements

GCW thanks the Canadian government for a NSERC Discovery Grant (RGPIN/435715-2013). IGH thanks the Canadian government for a NSERC Discovery Grant (RGPIN/355291), and the Canada Foundation for Innovation (Leading Edge Fund). JPS thanks Killam Trusts, and NSERC CGS. GCW, IGH, JPS, and AFE thank the NSERC CREATE DREAMS program for financial support. ADH would like to thank Dr. Jason Masuda and the St. Mary's Chemistry department for the use of their single crystal X-ray diffractometer.

Notes and references

[a] *Department of Physics, Dalhousie University, 1459 Oxford Street,Halifax, Nova Scotia, B3H 4R2, Canada. Email: ian.hill@dal.ca*
[b] *Department of Chemistry, Dalhousie University, 1459 Oxford Street,Halifax, Nova Scotia, B3H 4R2, Canada. Email: gregory.welch@dal.ca*

† Electronic Supplementary Information (ESI) available: [details of any supplementary information available should be included here].

See DOI: 10.1039/b000000x/

1. C. L. Chochos, N. Tagmatarchis, and V. G. Gregoriou, *RSC Adv.*, 2013, **3**, 7160.
2. A. Facchetti, *Mater. Today*, 2013, **16**, 123–132.
3. J. E. Anthony, *Chem. Mater.*, 2011, **23**, 583–590.
4. E. Kozma and M. Catellani, *Dyes Pigments*, 2013, **98**, 160–179.
5. C. Wang, H. Dong, W. Hu, Y. Liu, and D. Zhu, *Chem. Rev.*, 2012, **112**, 2208–2267.
6. P. M. Beaujuge and J. M. J. Fréchet, *J. Am. Chem. Soc.*, 2011, **133**, 20009–20029.
7. H. Yan, Z. Chen, Y. Zheng, C. Newman, J. R. Quinn, F. Dötz, M. Kastler, and A. Facchetti, *Nature*, 2009, **457**, 679–686.
8. R. H. Friend, R. W. Gymer, A. B. Holmes, J. H. Burroughes, R. N. Marks, C. Taliani, D. D. C. Bradley, D. A. D. Santos, J. L. Brédas, M. Lögdlund, and W. R. Salaneck, *Nature*, 1999, **397**, 121–128.
9. M. Stolar and T. Baumgartner, *Phys. Chem. Chem. Phys.*, 2013, **15**, 9007.
10. J. E. Anthony, A. Facchetti, M. Heeney, S. R. Marder, and X. Zhan, *Adv. Mater.*, 2010, **22**, 3876–3892.
11. H. Sirringhaus, P. J. Brown, R. H. Friend, M. M. Nielsen, K. Bechgaard, B. M. W. Langeveld-Voss, A. J. H. Spiering, R. a. J. Janssen, E. W. Meijer, P. Herwig, and D. M. de Leeuw, *Nature*, 1999, **401**, 685–688.
12. M. Mas-Torrent and C. Rovira, *Chem. Rev.*, 2011, **111**, 4833–4856.
13. T. Yamamoto, *NPG Asia Mater.*, 2010, **2**, 54–60.
14. J. Kim, *Pure Appl. Chem.*, 2002, **74**, 2031–2044.
15. G. C. Welch, R. C. Bakus, S. J. Teat, and G. C. Bazan, *J. Am. Chem. Soc.*, 2013, **135**, 2298–2305.
16. A. Mishra, C.-Q. Ma, and P. Bäuerle, *Chem. Rev.*, 2009, **109**, 1141–1276.
17. Y. Zhao, Y. Guo, and Y. Liu, *Adv. Mater.*, 2013, **25**, 5372–5391.
18. H. Klauk, *Chem. Soc. Rev.*, 2010, **39**, 2643.
19. Y. Qiao, Y. Guo, C. Yu, F. Zhang, W. Xu, Y. Liu, and D. Zhu, *J. Am. Chem. Soc.*, 2012, **134**, 4084–4087.
20. S. Dong, H. Zhang, L. Yang, M. Bai, Y. Yao, H. Chen, L. Gan, T. Yang, H. Jiang, S. Hou, L. Wan, and X. Guo, *Adv. Mater.*, 2012, **24**, 5576–5580.
21. S. Schols, L. V. Willigenburg, R. Müller, D. Bode, M. Debucquoy, S. D. Jonge, J. Genoe, P. Heremans, S. Lu, and A. Facchetti, *Appl. Phys. Lett.*, 2008, **93**, 263303.
22. M. Funahashi, F. Zhang, and N. Tamaoki, *Adv. Mater.*, 2007, **19**, 353–358.
23. X. Cai, C. P. Gerlach, and C. D. Frisbie, *J. Phys. Chem. C*, 2007, **111**, 452–456.
24. J. Nishida, S. Murakami, H. Tada, and Y. Yamashita, *Chem. Lett.*, 2006, **35**, 1236–1237.
25. F. Di Maria, P. Olivelli, M. Gazzano, A. Zanelli, M. Biasiucci, G. Gigli, D. Gentili, P. D'Angelo, M. Cavallini, and G. Barbarella, *J. Am. Chem. Soc.*, 2011, **133**, 8654–8661.
26. R. B. K. Siram, K. Tandy, M. Horecha, P. Formanek, M. Stamm, S. Gevorgyan, F. C. Krebs, A. Kiriy, P. Meredith, P. L. Burn, E. B. Namdas, and S. Patil, *J. Phys. Chem. C*, 2011, **115**, 14369–14376.
27. M.-C. Um, J. Kwak, J.-P. Hong, J. Kang, D. Y. Yoon, S. H. Lee, C. Lee, and J.-I. Hong, *J. Mater. Chem.*, 2008, **18**, 4698.
28. M. M. Payne, S. A. Odom, S. R. Parkin, and J. E. Anthony, *Org. Lett.*, 2004, **6**, 3325–3328.
29. M.-H. Yoon, S. A. DiBenedetto, A. Facchetti, and T. J. Marks, *J. Am. Chem. Soc.*, 2005, **127**, 1348–1349.
30. J. A. Letizia, S. Cronin, R. P. Ortiz, A. Facchetti, M. A. Ratner, and T. J. Marks, *Chem. – Eur. J.*, 2010, **16**, 1911–1928.
31. Y. Ie, K. Nishida, M. Karakawa, H. Tada, A. Asano, A. Saeki, S. Seki, and Y. Aso, *Chem. – Eur. J.*, 2011, **17**, 4750–4758.
32. Y. Ie, K. Nishida, M. Karakawa, H. Tada, and Y. Aso, *J. Org. Chem.*, 2011, **76**, 6604–6610.
33. B. Fu, J. Baltazar, Z. Hu, A.-T. Chien, S. Kumar, C. L. Henderson, D. M. Collard, and E. Reichmanis, *Chem. Mater.*, 2012, **24**, 4123–4133.
34. W. Elsawy, C.-L. Lee, S. Cho, S.-H. Oh, S.-H. Moon, A. Elbarbary, and J.-S. Lee, *Phys Chem Chem Phys*, 2013, **15**, 15193–15203.
35. J.-Y. Balandier, F. Quist, C. Amato, S. Bouzakraoui, J. Cornil, S. Sergeyev, and Y. Geerts, *Tetrahedron*, 2010, **66**, 9560 – 9572.
36. J. Li, X. Qiao, Y. Xiong, W. Hong, X. Gao, and H. Li, *J Mater Chem C*, 2013, **1**, 5128–5132.
37. Y.-M. Hwang, J. Ohshita, T. Mizumo, H. Yoshida, Y. Kunugi, and T. Sugioka, *Bull. Chem. Soc. Jpn.*, 2011, **84**, 1243–1247.
38. H. T. Black, A. Dadvand, S. Liu, V. S. Ashby, and D. F. Perepichka, *J Mater Chem C*, 2013, **1**, 260–267.
39. Z. Zuo, H. Sun, and X. Li, *Chin. J. Chem.*, 2012, **30**, 2401–2410.
40. T. Liu, K. Zhao, K. Liu, L. Ding, S. Yin, and Y. Fang, *J. Hazard. Mater.*, 2013, **246–247**, 52 – 60.
41. M. Durso, D. Gentili, C. Bettini, A. Zanelli, M. Cavallini, F. D. Angelis, M. G. Lobello, V. Biondo, M. Muccini, R. Capelli, and M. Melucci, *Chem. Commun.*, 2013, **49**, 4298–4300.
42. A. D. Hendsbee, C. M. Macaulay, and G. C. Welch, *Dyes Pigments*. DOI: 10.1016/j.dyepig.2013.10.046.
43. F. Kaneko, S. Honda, T. Fukami, K. Kato, T. Wakamatsu, K. Shinbo, and S. Kobayashi, *Thin Solid Films*, 1996, **284–285**, 417–419.
44. H. Meng, J. Zheng, A. J. Lovinger, B.-C. Wang, P. G. Van Patten, and Z. Bao, *Chem. Mater.*, 2003, **15**, 1778–1787.
45. Y. M. Sun, Y. Q. Ma, Y. Q. Liu, Y. Y. Lin, Z. Y. Wang, Y. Wang, C. A. Di, K. Xiao, X. M. Chen, W. F. Qiu, B. Zhang, G. Yu, W. P. Hu, and D. B. Zhu, *Adv. Funct. Mater.*, 2006, **16**, 426–432.
46. H. Tian, J. Wang, J. Shi, D. Yan, L. Wang, Y. Geng, and F. Wang, *J. Mater. Chem.*, 2005, **15**, 3026–3033.
47. Z. Duan, D. Hu, H. Ohuchi, M. Zhao, G. Zhao, and Y. Nishioka, *Synth. Met.*, 2012, **162**, 1292–1298.
48. S. Zhang, Y. Guo, H. Xi, C. Di, J. Yu, K. Zheng, R. Liu, X. Zhan, and Y. Liu, *Thin Solid Films*, 2009, **517**, 2968–2973.
1. C. L. Chochos, N. Tagmatarchis, and V. G. Gregoriou, *RSC Adv.*, 2013, **3**, 7160.
2. A. Facchetti, *Mater. Today*, 2013, **16**, 123–132.
3. J. E. Anthony, *Chem. Mater.*, 2011, **23**, 583–590.
4. E. Kozma and M. Catellani, *Dyes Pigments*, 2013, **98**, 160–179.
5. C. Wang, H. Dong, W. Hu, Y. Liu, and D. Zhu, *Chem. Rev.*, 2012, **112**, 2208–2267.
6. P. M. Beaujuge and J. M. J. Fréchet, *J. Am. Chem. Soc.*, 2011, **133**, 20009–20029.
7. H. Yan, Z. Chen, Y. Zheng, C. Newman, J. R. Quinn, F. Dötz, M. Kastler, and A. Facchetti, *Nature*, 2009, **457**, 679–686.

8. R. H. Friend, R. W. Gymer, A. B. Holmes, J. H. Burroughes, R. N. Marks, C. Taliani, D. D. C. Bradley, D. A. D. Santos, J. L. Brédas, M. Lögdlund, and W. R. Salaneck, *Nature*, 1999, **397**, 121–128.
9. M. Stolar and T. Baumgartner, *Phys. Chem. Chem. Phys.*, 2013, **15**, 9007.
10. J. E. Anthony, A. Facchetti, M. Heeney, S. R. Marder, and X. Zhan, *Adv. Mater.*, 2010, **22**, 3876–3892.
11. H. Sirringhaus, P. J. Brown, R. H. Friend, M. M. Nielsen, K. Bechgaard, B. M. W. Langeveld-Voss, A. J. H. Spiering, R. a. J. Janssen, E. W. Meijer, P. Herwig, and D. M. de Leeuw, *Nature*, 1999, **401**, 685–688.
12. M. Mas-Torrent and C. Rovira, *Chem. Rev.*, 2011, **111**, 4833–4856.
13. T. Yamamoto, *NPG Asia Mater.*, 2010, **2**, 54–60.
14. J. Kim, *Pure Appl. Chem.*, 2002, **74**, 2031–2044.
15. G. C. Welch, R. C. Bakus, S. J. Teat, and G. C. Bazan, *J. Am. Chem. Soc.*, 2013, **135**, 2298–2305.
16. A. Mishra, C.-Q. Ma, and P. Bäuerle, *Chem. Rev.*, 2009, **109**, 1141–1276.
17. Y. Zhao, Y. Guo, and Y. Liu, *Adv. Mater.*, 2013, **25**, 5372–5391.
18. H. Klauk, *Chem. Soc. Rev.*, 2010, **39**, 2643.
19. Y. Qiao, Y. Guo, C. Yu, F. Zhang, W. Xu, Y. Liu, and D. Zhu, *J. Am. Chem. Soc.*, 2012, **134**, 4084–4087.
20. S. Dong, H. Zhang, L. Yang, M. Bai, Y. Yao, H. Chen, L. Gan, T. Yang, H. Jiang, S. Hou, L. Wan, and X. Guo, *Adv. Mater.*, 2012, **24**, 5576–5580.
21. S. Schols, L. V. Willigenburg, R. Müller, D. Bode, M. Debucquoy, S. D. Jonge, J. Genoe, P. Heremans, S. Lu, and A. Facchetti, *Appl. Phys. Lett.*, 2008, **93**, 263303.
22. M. Funahashi, F. Zhang, and N. Tamaoki, *Adv. Mater.*, 2007, **19**, 353–358.
23. X. Cai, C. P. Gerlach, and C. D. Frisbie, *J. Phys. Chem. C*, 2007, **111**, 452–456.
24. J. Nishida, S. Murakami, H. Tada, and Y. Yamashita, *Chem. Lett.*, 2006, **35**, 1236–1237.
25. F. Di Maria, P. Olivelli, M. Gazzano, A. Zanelli, M. Biasiucci, G. Gigli, D. Gentili, P. D'Angelo, M. Cavallini, and G. Barbarella, *J. Am. Chem. Soc.*, 2011, **133**, 8654–8661.
26. R. B. K. Siram, K. Tandy, M. Horecha, P. Formanek, M. Stamm, S. Gevorgyan, F. C. Krebs, A. Kiriy, P. Meredith, P. L. Burn, E. B. Namdas, and S. Patil, *J. Phys. Chem. C*, 2011, **115**, 14369–14376.
27. M.-C. Um, J. Kwak, J.-P. Hong, J. Kang, D. Y. Yoon, S. H. Lee, C. Lee, and J.-I. Hong, *J. Mater. Chem.*, 2008, **18**, 4698.
28. M. M. Payne, S. A. Odom, S. R. Parkin, and J. E. Anthony, *Org. Lett.*, 2004, **6**, 3325–3328.
29. M.-H. Yoon, S. A. DiBenedetto, A. Facchetti, and T. J. Marks, *J. Am. Chem. Soc.*, 2005, **127**, 1348–1349.
30. J. A. Letizia, S. Cronin, R. P. Ortiz, A. Facchetti, M. A. Ratner, and T. J. Marks, *Chem. – Eur. J.*, 2010, **16**, 1911–1928.
31. Y. Ie, K. Nishida, M. Karakawa, H. Tada, A. Asano, A. Saeki, S. Seki, and Y. Aso, *Chem. – Eur. J.*, 2011, **17**, 4750–4758.
32. Y. Ie, K. Nishida, M. Karakawa, H. Tada, and Y. Aso, *J. Org. Chem.*, 2011, **76**, 6604–6610.
33. B. Fu, J. Baltazar, Z. Hu, A.-T. Chien, S. Kumar, C. L. Henderson, D. M. Collard, and E. Reichmanis, *Chem. Mater.*, 2012, **24**, 4123–4133.
34. W. Elsawy, C.-L. Lee, S. Cho, S.-H. Oh, S.-H. Moon, A. Elbarbary, and J.-S. Lee, *Phys Chem Chem Phys*, 2013, **15**, 15193–15203.
35. J.-Y. Balandier, F. Quist, C. Amato, S. Bouzakraoui, J. Cornil, S. Sergeyev, and Y. Geerts, *Tetrahedron*, 2010, **66**, 9560 – 9572.
36. J. Li, X. Qiao, Y. Xiong, W. Hong, X. Gao, and H. Li, *J Mater Chem C*, 2013, **1**, 5128–5132.
37. Y.-M. Hwang, J. Ohshita, T. Mizumo, H. Yoshida, Y. Kunugi, and T. Sugioka, *Bull. Chem. Soc. Jpn.*, 2011, **84**, 1243–1247.
38. H. T. Black, A. Dadvand, S. Liu, V. S. Ashby, and D. F. Perepichka, *J Mater Chem C*, 2013, **1**, 260–267.
39. Z. Zuo, H. Sun, and X. Li, *Chin. J. Chem.*, 2012, **30**, 2401–2410.
40. T. Liu, K. Zhao, K. Liu, L. Ding, S. Yin, and Y. Fang, *J. Hazard. Mater.*, 2013, **246–247**, 52 – 60.
41. M. Durso, D. Gentili, C. Bettini, A. Zanelli, M. Cavallini, F. D. Angelis, M. G. Lobello, V. Biondo, M. Muccini, R. Capelli, and M. Melucci, *Chem. Commun.*, 2013, **49**, 4298–4300.
42. A. D. Hendsbee, C. M. Macaulay, and G. C. Welch, *Dyes Pigments*. DOI: 10.1016/j.dyepig.2013.10.046.
43. F. Kaneko, S. Honda, T. Fukami, K. Kato, T. Wakamatsu, K. Shinbo, and S. Kobayashi, *Thin Solid Films*, 1996, **284–285**, 417–419.
44. H. Meng, J. Zheng, A. J. Lovinger, B.-C. Wang, P. G. Van Patten, and Z. Bao, *Chem. Mater.*, 2003, **15**, 1778–1787.
45. Y. M. Sun, Y. Q. Ma, Y. Q. Liu, Y. Y. Lin, Z. Y. Wang, Y. Wang, C. A. Di, K. Xiao, X. M. Chen, W. F. Qiu, B. Zhang, G. Yu, W. P. Hu, and D. B. Zhu, *Adv. Funct. Mater.*, 2006, **16**, 426–432.
46. H. Tian, J. Wang, J. Shi, D. Yan, L. Wang, Y. Geng, and F. Wang, *J. Mater. Chem.*, 2005, **15**, 3026–3033.
47. Z. Duan, D. Hu, H. Ohuchi, M. Zhao, G. Zhao, and Y. Nishioka, *Synth. Met.*, 2012, **162**, 1292–1298.
48. S. Zhang, Y. Guo, H. Xi, C. Di, J. Yu, K. Zheng, R. Liu, X. Zhan, and Y. Liu, *Thin Solid Films*, 2009, **517**, 2968–2973.
49. X. Li, B. K. C. Kjellander, J. E. Anthony, C. W. M. Bastiaansen, D. J. Broer, and G. H. Gelinck, *Adv. Funct. Mater.*, 2009, **19**, 3610–3617.
50. R. Capelli, F. Dinelli, S. Toffanin, F. Todescato, M. Murgia, M. Muccini, A. Facchetti, and T. J. Marks, *J. Phys. Chem. C*, 2008, **112**, 12993–12999.
51. M. Durso, C. Bettini, A. Zanelli, M. Gazzano, M. G. Lobello, F. De Angelis, V. Biondo, D. Gentili, R. Capelli, M. Cavallini, S. Toffanin, M. Muccini, and M. Melucci, *Org. Electron.*, 2013, **14**, 3089–3097.
52. L. E. Scriven and C. V. Sternling, *Nature*, 1960, **187**, 186–188.
53. G. R. Desiraju and A. Gavezzotti, *Acta Crystallogr. B*, 1989, **45**, 473–482.
54. M. D. Curtis, J. Cao, and J. W. Kampf, *J. Am. Chem. Soc.*, 2004, **126**, 4318–4328.
55. H. Dong, X. Fu, J. Liu, Z. Wang, and W. Hu, *Adv. Mater.*, 2013, **25**, 6158–6183.
56. T. Itoh, S. Aomori, M. Oh-e, M. Koden, and Y. Arakawa, *Synth. Met.*, 2012, **162**, 1264–1270.
57. P. J. Skabara, J.-B. Arlin, and Y. H. Geerts, *Adv. Mater.*, 2013, **25**, 1948–1954.
58. J. Zhang, L. Tan, W. Jiang, W. Hu, and Z. Wang, *J. Mater. Chem. C*, 2013, **1**, 3200–3206.
59. H. Thiem, P. Strohriegl, S. Setayesh, and D. de Leeuw, *Synth. Met.*, 2006, **156**, 582–589.
60. M. Tantiwiwat, A. Tamayo, N. Luu, X.-D. Dang, and T.-Q. Nguyen, *J. Phys. Chem. C*, 2008, **112**, 17402–17407.
61. J. Seo, S. Park, S. Nam, H. Kim, and Y. Kim, *Sci. Rep.*, 2013, **3**.
62. O. Thiebaut, H. Bock, and E. Grelet, *J. Am. Chem. Soc.*, 2010, **132**, 6886–6887.
63. E. Beltrán, J. L. Serrano, T. Sierra, and R. Giménez, *J. Mater. Chem.*, 2012, **22**, 7797–7805.
64. M. O'Neill and S. M. Kelly, *Adv. Mater.*, 2011, **23**, 566–584.
65. F. Araoka, S. Masuko, A. Kogure, D. Miyajima, T. Aida, and H. Takezoe, *Adv. Mater.*, 2013, **25**, 4014–4017.
66. H. Fukagawa, H. Yamane, T. Kataoka, S. Kera, M. Nakamura, K. Kudo, and N. Ueno, *Phys. Rev. B*, 2006, **73**, 245310.
67. N. Koch, I. Salzmann, R. L. Johnson, J. Pflaum, R. Friedlein, and J. P. Rabe, *Org. Electron.*, 2006, **7**, 537–545.

68. K. Ihm, B. Kim, T.-H. Kang, K.-J. Kim, M. H. Joo, T. H. Kim, S. S. Yoon, and S. Chung, *Appl. Phys. Lett.*, 2006, **89**, 033504.
69. S. Duhm, G. Heimel, I. Salzmann, H. Glowatzki, R. L. Johnson, A. Vollmer, J. P. Rabe, and N. Koch, *Nat. Mater.*, 2008, **7**, 326–332.
70. M. J. Frisch, G. W. Trucks, H. B. Schlegel, G. E. Scuseria, M. A. Robb, J. R. Cheeseman, G. Scalmani, V. Barone, B. Mennucci, G. A. Petersson, H. Nakatsuji, M. Caricato, X. Li, H. P. Hratchian, A. F. Izmaylov, J. Bloino, G. Zheng, J. L. Sonnenberg, M. Hada, M. Ehara, K. Toyota, R. Fukada, J. Hasegawa, M. Ishida, T. Nakajima, Y. Honda, O. Kitao, H. Nakai, T. Vreven, J. A. Montgomery, J. E. Peralta, F. Ogliaro, M. Bearpark, J. J. Heyd, E. Brothers, K. Kudin, V. N. Staroverov, R. Kobayashi, J. Normand, K. Raghavachari, A. Rendell, J. C. Burant, S. S. Iyengar, J. Tomasi, M. Cossi, N. Rega, N. J. Mllam, M. Klene, J. E. Knox, J. B. Cross, V. Bakken, C. Adamo, J. Jaramillo, R. Gomperts, R. E. Stratmann, O. Yazyev, A. J. Austin, R. Cammi, C. Pomelli, J. W. Ochterski, R. L. Martin, K. Morokuma, V. G. Zakrzewski, G. A. Voth, P. Salvador, J. J. Dannenberg, S. Dapprich, A. D. Daniels, O. Farkas, J. B. Foresman, J. V. Ortiz, J. Cioslowski, and D. J. Fox, *Gaussian 09*, Gaussian Inc., Wallingford CT, 2009.

Table 1 Summary of solution and film optical data, for compounds **1**-**5**.

Compound	Solution		Film		PL
	λ_{max} [nm]	λ_{onset} [nm]	λ_{max} [nm]	λ_{onset} [nm]	λ_{em} [nm]
1	424	486	385	515	508
2	425	486	390	515	515
3	428	494	400	535	523
4	450	515	395	540	538
5	390	440	375	530	466

Table 2 Summary of thermal, electronic, DFT and FET device data for compounds **1**-**5.**

Compound	UPS				DFT			DSC		FET		
	IE [eV]	HOMO[a] [eV]	LUMO[b] [eV]	E_g[c] [eV]	HOMO[d] [eV]	LUMO[d] [eV]	E_g[d] [eV]	T_m [°C]	T_c [°C]	μ_e [$cm^2V^{-1}s^{-1}$]	V_{th} [V]	I_{on}/I_{off}
1	6.1	-6.1	-3.7	2.41	-6.03	-3.07	2.96	221	208	7.6×10^{-2}	28	10^5
2	6.3	-6.3	-3.9	2.41	x	x	x	230	215	2.1×10^{-1}	28	10^5
3	5.8	-5.8	-3.5	2.32	x	x	x	279	243	1.5×10^{-1}	23	10^5
4	5.7	-5.7	-3.4	2.30	-5.76	-3.04	2.71	245	234	2.3×10^{-3}	45	10^1
5	6.5	-6.5	-4.2	2.34	-6.48	-3.09	3.39	204	191	6.3×10^{-2}	23	10^4

[a] HOMO = -IE; [b]LUMO = HOMO + E_g; [c]E_g = 1240/ $\lambda_{onset,thin\ film}$; [d]From DFT calculations, details in section 2.7 of this document

Fig. 1 Chemical structures for compounds **1-5**.

Fig. 2 UV-Vis absorbance spectra of compounds **1**-**5** in chloroform solution (solid) and thin film (dotted lines).

Fig. 3 Optical microscope images a) compound **1** drop cast from a 58 °C, 50 mg mL^{-1} solution, b) compound **2** drop cast from a 58 °C, 13.2 mg mL^{-1} solution, c) compound **3** drop cast from a 58 °C, 1.15 mg mL^{-1} solution, d) compound **1** drop cast from a 58 °C 10 mg mL^{-1} solution, e) compound **2** drop cast from a 58 °C 2.6 mg mL^{-1} solution f) close up image of compound **3** drop cast from a 58 °C 1.15 mg mL^{-1} solution. Thin film X-ray diffraction patterns g) compound **1**, h) compound **2**, i) compound **3**.

Fig. 4 Crystal structures of **1** and **2**: (a) **1** viewed along the a-axis showing γ-structure, and pitch and roll angles and spacing between π-planes indicating π-stacking geometry, (b) **2** viewed along the c-axis showing 1D columnar stacking, and pitch and roll angles and spacing between π-planes indicating π-stacking geometry, (c) rotated view of **1** with π-planes highlighted in blue and yellow, (d) rotated view of **2** with π-planes highlighted in blue and purple.

Fig. 5 Results from B3LYP/6-31G(d,p) calculations comparing **5**(a), **1** (b), and **4**(c) structures. Angle between adjacent ring planes (degrees, °) shown in black text (top structures). Dipole moment vectors and magnitudes (Debyes, D) are shown in green. HOMO/LUMO molecular orbital diagrams and energies (eV) are shown below.

Fig. 6 Saturation transfer curves for OFETs made from compounds **1**-**5**.

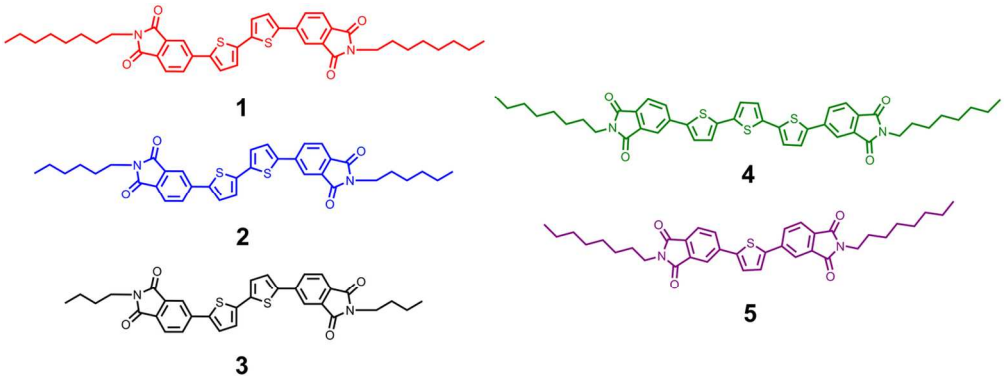

Fig. 1 Chemical structures for compounds **1**-**5**.
63x24mm (600 x 600 DPI)

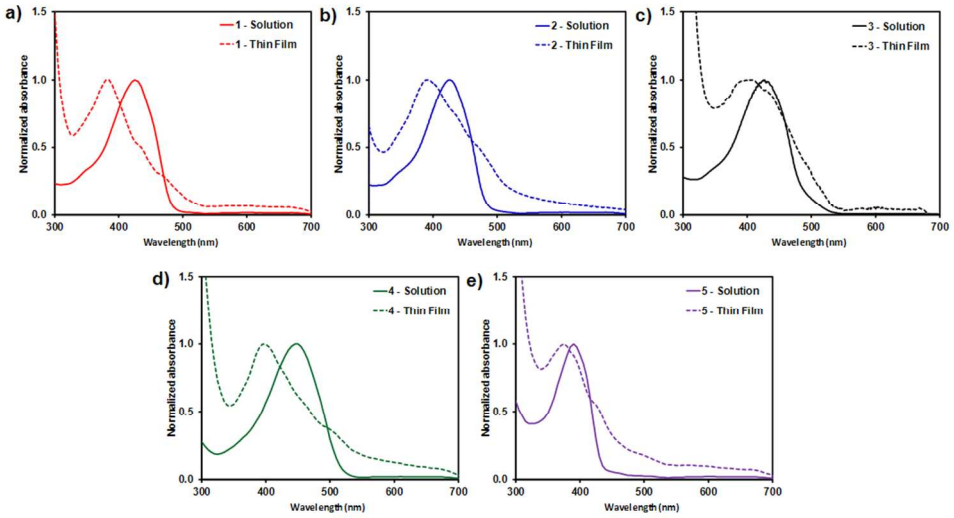

Fig. 2 UV-Vis absorbance spectra of compounds **1-5** in chloroform solution (solid) and thin film (dotted lines).<
299x157mm (96 x 96 DPI)

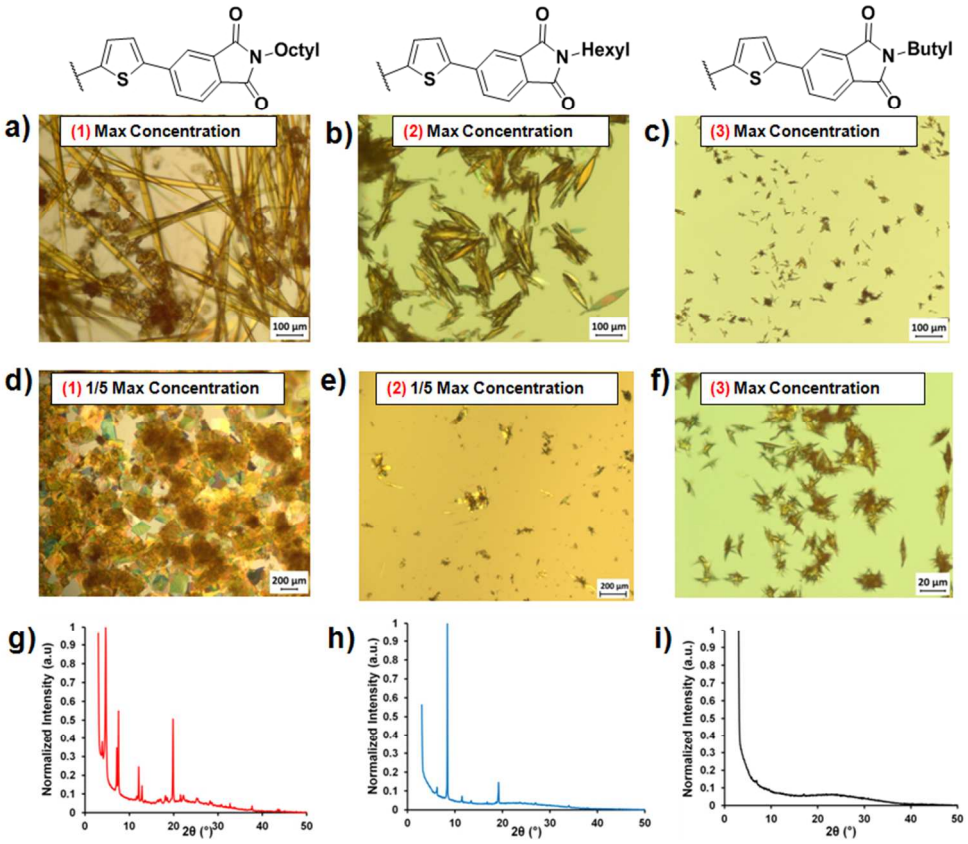

Fig. 3 Optical microscope images a) compound **1** drop cast from a 58 °C, 50 mg mL^{-1} solution, b) compound **2** drop cast from a 58 °C, 13.2 mg mL^{-1} solution, c) compound **3** drop cast from a 58 °C, 1.15 mg mL^{-1} solution, d) compound **1** drop cast from a 58 °C 10 mg mL^{-1} solution, e) compound **2** drop cast from a 58 °C 2.6 mg mL^{-1} solution f) close up image of compound **3** drop cast from a 58 °C 1.15 mg mL^{-1} solution. Thin film X-ray diffraction patterns g) compound **1**, h) compound **2**, i) compound **3**.
239x200mm (96 x 96 DPI)

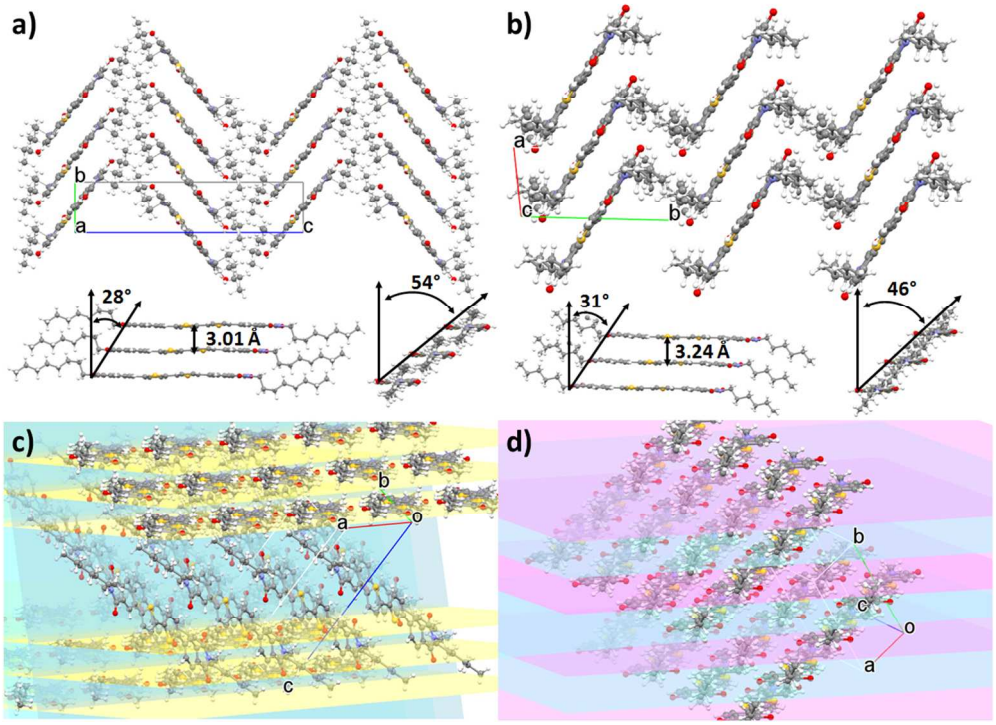

Fig. 4 Crystal structures of **1** and **2**: (a) **1** viewed along the a-axis showing γ-structure, and pitch and roll angles and spacing between π-planes indicating π-stacking geometry, (b) **2** viewed along the c-axis showing 1D columnar stacking, and pitch and roll angles and spacing between π-planes indicating π-stacking geometry, (c) rotated view of **1** with π-planes highlighted in blue and yellow, (d) rotated view of **2** with π-planes highlighted in blue and purple.
334x242mm (96 x 96 DPI)

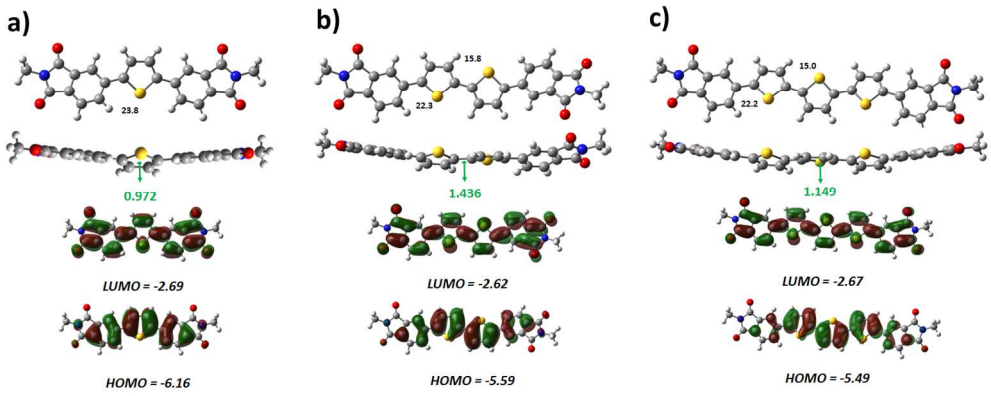

Fig. 5 Results from B3LYP/6-31G(d,p) calculations comparing **5**(a), **1** (b), and **4**(c) structures. Angle between adjacent ring planes (degrees, °) shown in black text (top structures). Dipole moment vectors and magnitudes (Debyes, D) are shown in green. HOMO/LUMO molecular orbital diagrams and energies (eV) are shown below.
437x177mm (96 x 96 DPI)

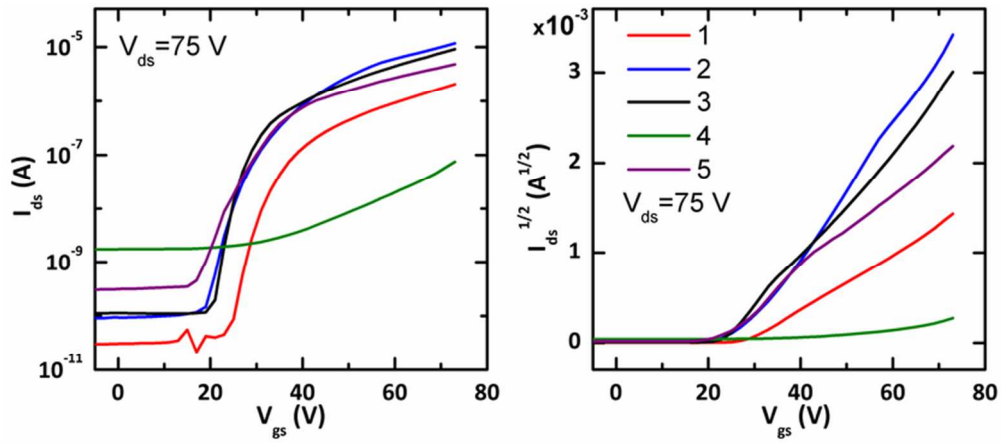

Fig. 6 Saturation transfer curves for OFETs made from compounds **1**-**5**.
70x30mm (300 x 300 DPI)